

# Ultrasound Image Guided and Mixed Reality-Based Surgical System With Real-Time Soft Tissue Deformation Computing for Robotic Cervical Pedicle Screw Placement

Puxun Tu , Chunxia Qin , Yan Guo , Dongyuan Li, Abel J. Lungu , Huixiang Wang, and Xiaojun Chen , Member, IEEE

**Abstract—Objective:** Cervical pedicle screw (CPS) placement surgery remains technically demanding due to the complicated anatomy with neurovascular structures. State-of-the-art surgical navigation or robotic systems still suffer from the problem of hand-eye coordination and soft tissue deformation. In this study, we aim at tracking the intraoperative soft tissue deformation and constructing a virtual-physical fusion surgical scene, and integrating them into the robotic system for CPS placement surgery. **Methods:** Firstly, we propose a real-time deformation computation method based on the prior shape model and intraoperative partial information acquired from ultrasound images. According to the generated posterior shape, the structure representation of deformed target tissue gets updated continuously. Secondly, a hand tremble compensation method is proposed to improve the accuracy and robustness of the virtual-physical calibration procedure, and a mixed reality based surgical scene is further constructed for CPS placement surgery. Thirdly, we integrate the soft tissue deformation method and virtual-physical fusion method into our previously proposed surgical robotic system, and the

surgical workflow for CPS placement surgery is introduced. **Results:** We conducted phantom and animal experiments to evaluate the feasibility and accuracy of the proposed system. Our system yielded a mean surface distance error of  $1.52 \pm 0.43$  mm for soft tissue deformation computing, and an average distance deviation of  $1.04 \pm 0.27$  mm for CPS placement. **Conclusion:** Results demonstrate that our system involves tremendous clinical application potential. **Significance:** Our proposed system promotes the efficiency and safety of the CPS placement surgery.

**Index Terms**—Image guided surgery, mixed reality, ultrasound image, orthopedic surgery.

## I. INTRODUCTION

CERVICAL pedicle screw (CPS) has become a superior choice for cervical surgery because of its stable biomechanical property and strong fixation performance [1], [2]. It is widely employed in the treatment of multifarious cervical spondylosis and cervical injuries, such as trauma, neoplastic destruction, degenerative diseases, and kyphosis correction [3]. Generally, the standard-of-care for CPS surgery is intermittent fluoroscopy guidance. However, its free-hand procedure involves various limitations including prolonged operation time, considerable radiation exposure and high complication rate [4].

The major clinical challenges for surgeons to perform the CPS surgery are summarized as follows: the cervical spine consists of 7 vertebrae with intricate anatomic structure and small osseous morphometrics [5]. The critical neurovascular structures around the cervical region boost the intraoperative risks of vertebral artery and nerve root injury [6]. Moreover, the surgeon's visibility range during operation is limited, thus the treatment result is highly associated with the surgeon's proficient knowledge of anatomic structure [7].

Recent decades have witnessed the rapid development of surgical navigation and surgical robotic systems for CPS surgery. Several surgical navigation systems have been applied recently, e.g. the preoperative CT-based navigation system [8], the C-arm-based intraoperative navigation system [9], the O-arm-based 3D navigation system [10]. Such systems can provide surgeons with real-time stereoscopic feedback of surgical tool's position

Manuscript received August 12, 2021; revised December 18, 2021; accepted January 31, 2022. Date of publication February 14, 2022; date of current version July 19, 2022. This work was supported in part by the National Natural Science Foundation of China under Grants 81971709, M-0019, and 82011530141, in part by the Foundation of Science and Technology Commission of Shanghai Municipality under Grant 19510712200 and 20490740700, in part by the Shanghai Jiao Tong University Foundation on Medical and Technological Joint Science Research under Grants YG2019ZDA06, YG2021ZD21, YG2021QN72, and YG2022QN056, in part by the 2020 Key Research Project of Xiamen Municipal Government under Grant 3502Z20201030, and in part by the Seed Fund of Medical and Technological Joint Research, Engineering Research Center of Digital Medicine, Ministry of Education of China under Grant 20210406. (*Puxun Tu and Chunxia Qin are co-first authors.*) (*Corresponding author:* Xiaojun Chen.)

Puxun Tu, Yan Guo, Dongyuan Li, and Abel J. Lungu are with the Institute of Biomedical Manufacturing and Life Quality Engineering, School of Mechanical Engineering, Shanghai Jiao Tong University, China.

Chunxia Qin is with the School of Biomedical Engineering, Shanghai Jiao Tong University, China, and also with the School of Mechanical Engineering, Shanghai Jiao Tong University, China.

Huixiang Wang is with the Department of Orthopedics, Shanghai Jiao Tong University Affiliated Sixth People's Hospital, China.

Xiaojun Chen is with the School of Mechanical Engineering, Shanghai Jiao Tong University, Shanghai 200240, China, and also with the Institute of Medical Robotics, Shanghai Jiao Tong University, Shanghai 200240, China (e-mail: xiaojunchen@sjtu.edu.cn).

Digital Object Identifier 10.1109/TBME.2022.3150952

0018-9294 © 2022 IEEE. Personal use is permitted, but republication/redistribution requires IEEE permission.  
See <https://www.ieee.org/publications/rights/index.html> for more information.

relative to the segmented cervical vertebrae, enhanced preoperative planning information, and manual operation guidance. As reported in [11], the use of 3D navigation systems has been a great advancement to surgical safety, intraoperative control, and learning curve. Also, the effective use of surgical robots in spine surgery has been demonstrated by literature. Surgical robots applied in spine surgery can be classified into supervisory controlled systems, tele-surgical robotic systems, and shared-control robotic systems [12]. With the function of simultaneous control by surgeons and the robot itself, the application of shared-control robots for spine surgery becomes mainstream. Many reports have demonstrated that commercially available robotic systems, including Mazor X Stealth [13], ExcelsiusGPS robotic system [14], and TianJi Robot [15] can significantly improve accuracy and reduce fatigue.

Though achieving certain results, existing computer assisted systems for CPS surgery still face several challenges. Firstly, the deformation of neurovascular structures increases the intraoperative risks. Due to the cervical movement, surgical instruments pressing, and ultrasound (US) transducer pressure, the deformation of the soft tissues are inevitable and unpredictable. If the deformed soft tissues interfere with the preoperative planning path, some severe neurovascular injuries may happen. A previous study reported that three vertebral artery injuries, five deaths, and one stroke happened in 426 patients with free-hand or navigation guided C2 pars pedicle screw placement [16]. Secondly, surgeons still suffer from hand-eye coordination problems. Surgeons have to switch their view between the 2D navigation display and the surgical site during navigation [17], resulting in an intermittent operation.

To track the intraoperative deformed tissues, some non-rigid registration based or finite-element based methods using US images have been recently proposed. Chen *et al.* [18] proposed a system to update the tissue structure based on calibrated US images and two-level surface warping for minimally invasive surgery. The phantom experiment illustrated that the accuracy for structure updating was 92.86%. However, the anatomical landmarks for tissue updating were manually selected, thus no continuous updating was supported during navigation. In another study conducted by Samei *et al.* [19], an effective registration method using 3D and 2.5D transrectal ultrasound images was proposed for robot-assisted laparoscopic radical prostatectomy. The soft tissue model can be updated with the finite-element model based registration information. Though it holds tremendous potential for real-time rendering, its applicable value for complicated anatomical structures (e.g. head-neck region) requires further evaluation.

To solve the hand-eye coordination problem, some ingenious navigation systems based on augmented reality (AR) or mixed reality (MR) were proposed for spine surgery. Navab *et al.* [20] presented an advanced camera augmented mobile C-arm system, which can augment the regular X-ray by video image overlay, and its robust performance in vertebroplasty procedure was proved. Ma *et al.* [21] present a novel AR navigation system based on an integral videography device and ultrasound images. With in site visualization, this glass-free 3D system can achieve acceptable accuracy. However, the finite visualization

range and visualization quality limit its clinical acceptance. An alternative is to use the optical see-through head-mounted display (OST-HMD) as proposed by Liebmann *et al.* [22], where in situ visualization and dynamic virtual-physical fusion are provided for pedicle screw placement surgery. The major drawback of the MR-based navigation system is that the registration accuracy needs improvement, especially in the depth direction [23]. Besides, existing AR and MR-based navigation systems applied in spine surgery all assume that the anatomical features are rigid and do not deform during surgery.

To sum up, existing non-rigid registration based or finite-element based methods can not achieve real-time deformation. Besides, existing MR fusion methods need to improve the accuracy and robustness, and lack an enduring solution for CPS placement integrated with deformation tracking.

In this study, we proposed a posterior shape model based deformation computing method and a novel virtual-physical fusion method, and integrated them into our previously self-developed surgical robotic system. The main contributions of this study can be summarized as follows

- 1) We proposed a soft tissue deformation computing and tracking algorithm. Feature points in the US images and intersection points in the prior shape model are acquired and matched automatically, and the posterior distribution is computed to update the soft tissue in real-time.

- 2) We proposed an interactive virtual-physical calibration method based on hand tremble compensation, with improved calibration accuracy and robustness. An MR-based surgical scene was further constructed to superpose the virtual components on their physical counterparts.

## II. METHODS

In this section, we mainly introduce the soft tissue deformation computing method and the virtual-physical fusion method. By conducting the spatial and temporal calibration procedures, the US images can be transformed into the local coordinate system of the statistical shape model (SSM). The posterior shape can be computed to update the shape representation of the soft target based on the extracted information from 2D US images and its correspondence with SSM, which will be illustrated in Section II.B. To realize the virtual-physical fusion of the soft and hard tissues around the cervical region, a hand trembled compensation algorithm is proposed with improved accuracy and robustness, which will be illustrated in Section II.C. The aforementioned technologies will be integrated into the surgical robotic system to improve the safety and stability of the CPS placement surgery, which will be illustrated in Section II.D.

### A. System Registration and Calibration

To realize the soft tissue deformation tracking in the mixed reality surgical environment, some essential registration and calibration procedures need to be conducted. As illustrated in Fig. 1(a), two transformation matrix chains are involved, and they are connected through the optical tracker coordinate system.

To superpose the virtual cervical vertebrae, preoperative planning path, and neurovascular tissues on the surgical site

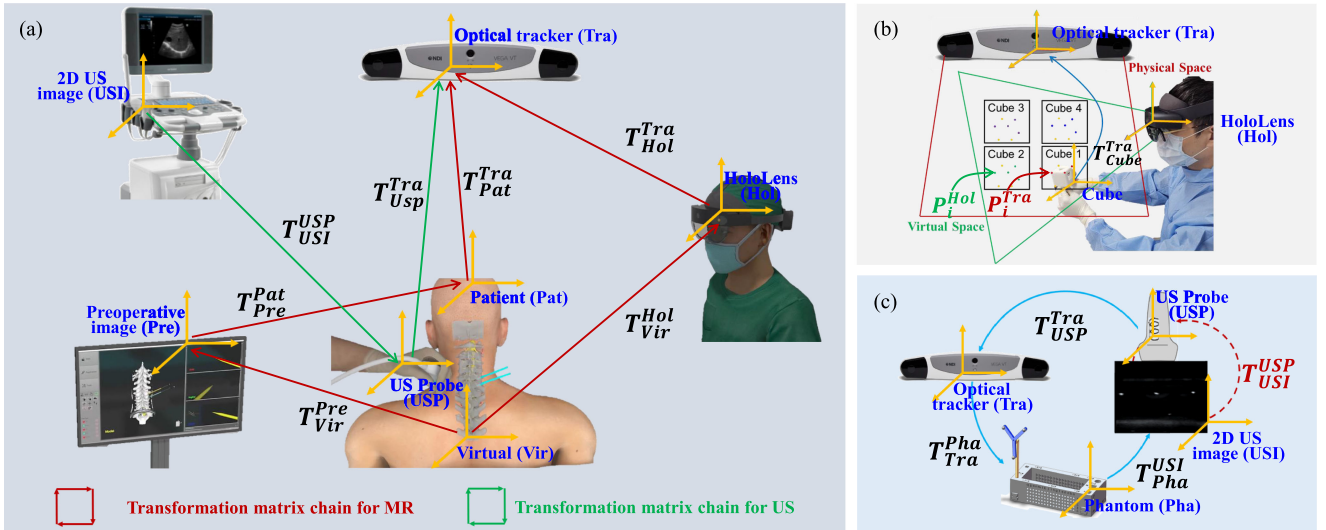


**Fig. 1.** Essential coordinate systems and transformation matrices involved in this study. (a) The closed transformation matrix chains for MR and US. (b) Our proposed interactive virtual-physical calibration procedure. (c) The 2D US calibration procedure. An N-wire phantom is used to provide corresponding points for the 2D US image coordinate system  $\{USI\}$  and the US probe coordinate system  $\{USP\}$  [27].

accurately, the transformation matrix  $T_{Vir}^{Hol}$  from the virtual coordinate system  $\{Vir\}$  to the HoloLens coordinate system  $\{Hol\}$  requires to be obtained in real time. As shown in Fig. 1(a), the matrix chain for MR gets closed to compute

$$T_{Vir}^{Hol} = (T_{Hol}^{Tra})^{-1} * T_{Pat}^{Tra} * T_{Pre}^{Pat} * T_{Vir}^{Pre} \quad (1)$$

where  $T_{Pat}^{Tra}$  represents the transformation matrix from patient coordinate system  $\{Pat\}$  to the optical tracker coordinate system  $\{Tra\}$ , which can be obtained in real time by tracking the optical reference frame attached on the patient.  $T_{Vir}^{Pre}$  represents the left-right hand transformation matrix that transforms the constructed mesh model from virtual coordinate system  $\{Vir\}$  to preoperative image coordinate system  $\{Pre\}$ .  $T_{Pre}^{Pat}$  represents the image-patient registration matrix that can be computed via landmark based approaches [24]. The initial virtual-physical calibration matrix  $T_{Hol}^{Tra}$  can be obtained using our preliminary proposed calibration cube [25]. As shown in Fig. 1(b),  $P_i^{Tra}$  and  $P_i^{Hol}$  represent the  $i$ -th 3D fiducial markers with respect to  $\{Tra\}$  and  $\{Hol\}$ , respectively.  $P_i^{Hol}$  is pre-defined in the holographic scene. These virtual fiducial markers in the user's view can remain stable thanks to the simultaneous localization and mapping technology.  $P_i^{Tra}$  is equal to  $T_{Cube}^{Tra} * P_i^{Ver}$ , where  $T_{Cube}^{Tra}$  represents the transformation matrix from the optical reference attached on the calibration cube  $\{Cube\}$  to  $\{Tra\}$ . And  $P_i^{Ver}$  represents the  $i$ -th 3D vertex point of  $\{Cube\}$ , which can be obtained via the pivoting procedure. To this end, the corresponding relationship of points between  $\{Tra\}$  and  $\{Hol\}$  can be expressed as

$$T_{Cube}^{Tra} * P_i^{Ver} = T_{Hol}^{Tra} * P_i^{Hol} \quad (2)$$

The objective function that minimizes the reprojection error can be derived as

$$\min \sum_{i=1}^N \left\| (T_{Hol}^{Tra})^{-1} * T_{Cube}^{Tra} * P_i^{Ver} - P_i^{Hol} \right\|^2 \quad (3)$$

where  $N$  is the fiducial points number for the calibration,  $\|\cdot\|^2$  represents the Frobenius norm. Based on the aforementioned objective function, the affine transformation (with 12 unknown parameters) between  $\{Tra\}$  and  $\{Hol\}$  can be computed using the Direct Linear Transformation algorithm [26].

To obtain the position of the 2D US image relative to  $\{Pre\}$  in real time, the 2D US image coordinate system  $\{USI\}$  should be transformed into  $\{Pre\}$ . As shown in Fig. 1(a), the transformation matrix  $T_{USI}^{Pre}$  can be computed as

$$T_{USI}^{Pre} = T_{USI}^{USP} * T_{USP}^{Tra} * (T_{Pat}^{Tra})^{-1} * (T_{Pre}^{Pat})^{-1} \quad (4)$$

where  $T_{USP}^{Tra}$  can be obtained in real time by tracking the optical reference frame attached on the US probe. As shown in Fig. 1(c), the calibration matrix  $T_{USI}^{USP}$  can be computed using the improved N-wire phantom-based freehand US calibration method [27].

To correlate the timestamps caused by different hardware components, a temporal calibration procedure is also conducted. By collecting tracking and US imaging data with a quasi-periodic pattern, the time offset between the US image stream and the optical tracking stream can be obtained [28].

## B. Real-Time Soft Tissue Deformation Computing

The essence of soft tissue deformation computing is to obtain the deformation field relative to  $\{Pre\}$ . To realize real-time soft tissue deformation tracking, we proposed a posterior shape model based soft tissue updating method using intraoperative US images, which proceeds as follows:

1) *PCA-Based SSM Model Generation*: With a set of CT images in the head and neck region, the critical soft tissue can be segmented and reconstructed (Fig. 2(a)). Each example shape

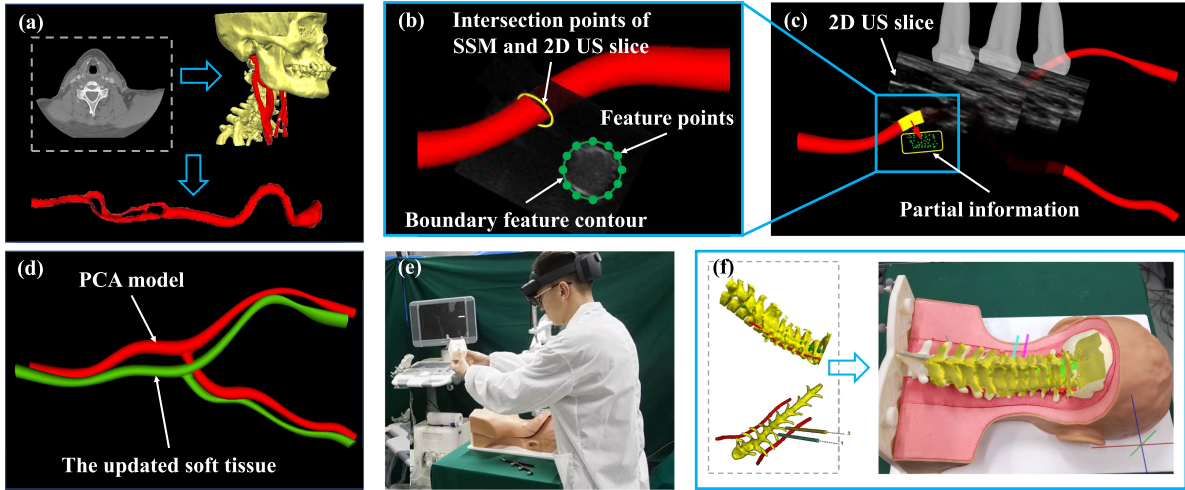


**Fig. 2.** (a) Segment and reconstruct the tissues, and generate the SSM. (b) The acquisition procedure of ultrasound features and their intersection points. (c) The collection of intraoperative partial information and its corresponding information in the PCA model. (d) Obtain the displacement field and update the soft tissue. (e) The virtual-physical calibration procedure. (f) Mixed reality scene construction.

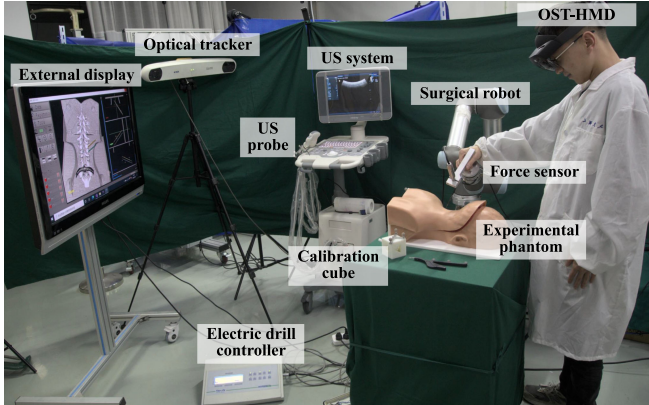


**Fig. 3.** The hardware components of the integrated system.

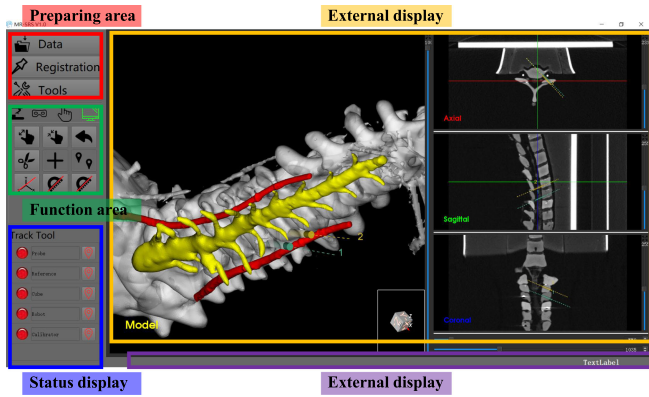


**Fig. 4.** The integrated software for CPS placement surgery.

$v_i \in \mathbb{R}^{N \times 3}$  can be represented as

$$v_i = (f^i\{P_1\}, \dots, f^i\{P_N\}) = (v_{i,1}^X, v_{i,1}^Y, v_{i,1}^Z, \dots, v_{i,N}^X, v_{i,N}^Y, v_{i,N}^Z)^T \quad (5)$$

where  $N$  is the points number of  $v_i$ ,  $f^i\{\cdot\} : \mathbb{R}^3 \rightarrow \mathbb{R}^3$  represents the function that matches each  $P_i$  to its corresponding point on

the reference mesh  $v_{ref}$ ,  $(v_{i,j}^X, v_{i,j}^Y, v_{i,j}^Z)$  represents the coordinate system of  $j - th$  vertex.

The sample mean of these shapes is as  $\bar{v} = (\sum_{i=1}^n v_i)/n$ , and the covariance matrix is defined as  $\Sigma = (\sum_{i=1}^n (v_i - \bar{v})^T)(v_i - \bar{v})/n$ . With eigenvalue decomposition,  $\Sigma$  can be expanded to  $\Sigma = UD^2U^T$ , where  $U \in \mathbb{R}^{N \times 3 \times n}$  is composed of principal components, and  $D^2$  denotes the variance representation of the principal components. Then the PCA model  $V$  can then be represented as

$$V = (v_1, \dots, v_n) = \bar{v} + \sum_{i=1}^n \alpha_i \lambda_i u_i = \bar{v} + Q\alpha \quad (6)$$

where  $\lambda_i$  is an entry in the diagonal matrix  $D^2$ ,  $u_i$  is the  $i - th$  column in  $U$ ,  $Q = q_i, i = 1, \dots, N \in \mathbb{R}^{n \times 3 \times N}$  represents these principal components, and  $\alpha \in \mathbb{R}^n$  represents the coefficient vector and follow a standard normal distribution  $\alpha \sim N(0, I_n)$ .

2) *Soft Tissue Computing With Partial Information:* The conditional distributions of target shape are inferred based on the partial information extracted from intraoperative US slices (Fig. 2(c)). The intraoperative partial information is defined as  $V^p = (v_1^p, \dots, v_k^p) \in \mathbb{R}^k$ , where  $k$  represents the entries number of  $V^p$ . Let  $\bar{v}^p \in \mathbb{R}^k$  denote the corresponding entries in  $\bar{v}$ , and  $Q^p \in \mathbb{R}^{k \times n}$  denote the corresponding sub-matrix in  $Q$ .  $V^p$  can then be represented as [30]

$$V^p = \bar{v}^p + Q^p\alpha + \varepsilon \quad (7)$$

where the noise parameter  $\varepsilon \sim N(0, \sigma^2 I_k)$ .

We defined the correspondence of  $V^p$  in  $V$  as  $V^{model} = (v_1^{model}, \dots, v_j^{model})$ . The align procedure that matches each entry of  $V^p$  with  $V^{model}$  is challenging but essential. The algorithm for partial information acquisition and correspondence is as Algorithm 1.

A nearly arc length parameterization method is used to interpolate the raw feature points  $\tilde{P}_i^{fea}$  and raw intersection points  $\tilde{P}_i^{Int}$  (Fig. 2(b)) to the same number of points. The boundary feature contour is defined as  $\Gamma^{fea} : r = r(t) =$

**Algorithm 1:** Prior model and partial information based deformation computation algorithm.

**Input:** The calibrated 2D US frames  $I^{Slice} = I_{i=1,\dots,L}$  and the PCA-based shape model  $V$ .

**Output:** The mean shape  $\bar{v}_p$  and the covariance matrix  $\Sigma_p$  of the generated posterior shape model.

**(a) Initialization**

- 1) Initialize  $V^p$  and  $V^{model}$  to zero.
- 2) Assign  $D^{Thr}$  (the threshold value for updating) to  $1.2\text{ mm}$ .

**(b) Image transformation**

- 1) Align  $I_i$  to  $\{Pre\}$  using Eq. (4).

**(c) Feature points and intersection points acquisition**

- 1) Extract the initial feature points

$\tilde{P}_i^{fea} = \{P_{i,\tilde{m}}\}_{\tilde{m}=1,\dots,\tilde{M}}$  from the US frame  $I_\lambda$  via the Mask R-CNN network [29].

- 2) Compute the intersection contour between image slice  $I_\lambda$  and prior shape  $V$ , and extract the raw intersection points  $P_i^{Int} = \{P_{i,\tilde{n}}\}_{\tilde{n}=1,\dots,\tilde{N}}$ .

- 3) By the nearly arc length parameterization algorithm (Eq. (8)),  $\hat{P}_i^{Tra}$  and  $\hat{P}_i^{Int}$  are interpolated to

$P_i^{fea} = \{P_{i,m}\}_{m=1,\dots,K}$  and  $P_i^{Int} = \{P_{i,n}\}_{n=1,\dots,K}$ , respectively. Here,  $K$  is 15.

**(d) Update  $V^p$  and  $V^{model}$**

- 1) For each image frame, compute the smallest Euclidean distance  $D_i^{fea}$  between  $P_i^{fea}$  and each entry of  $V^p$ , If  $D_i^{fea} < D^{Thr}$ ,

Replace the corresponding entry in  $V^p$  with  $P_i^{fea}$ , and replace the corresponding entry in  $V^{model}$  with  $P_i^{Int}$ . Else,

Add  $P_i^{fea}$  as a new entry for  $V^p$ , and add  $P_i^{Int}$  as a new entry for  $V^{model}$ .

**(e) Compute the posterior distribution**

- 1) Using Bayes' rule, the posterior distribution  $p(V|V^p)$  is computed using Eq. (9),  $\bar{v}_p$  is computed using Eq. (10), and  $\Sigma_p$  is computed using Eq. (11).

- 2) If  $P_i^{fea}$  is null,

Stop interaction and stop updating.

else,

Let  $i = i + 1$  and iterate to step (b).

$x(t), y(t), z(t)$ ,  $t_s \leq t \leq t_e$ . The arc length corresponding to each  $t_i \in [t_s, t_e]$  is  $S_i = S(t_i) = \int_{t_s}^t |r'(t)| dt$ . We define a linear rational function to piecewise approximate the arc length as

$$s_i(t) = \frac{W_{i-1}S_{i-1}(t_i - t) + W_iS_i(t - t_{i-1})}{W_{i-1}(t_i - t) + W_i(t - t_{i-1})}, \quad i = 1, \dots, n \quad (8)$$

where  $W_i = \frac{\Delta S_i / \Delta t_i}{\Delta S_{i+1} / \Delta t_{i+1}} W_{i-1}$ ,  $\Delta S_i = S_i - S_{i-1}$ ,  $\Delta t_i = t_i - t_{i-1}$ . The approximate arc length parameterized function can be used to compute  $P_i^{fea}$  and  $P_i^{Int}$ . With updated  $V^p$  and  $V^{model}$ , the posterior distribution can be computed as [30]

$$p(V|V^p) =: N(\bar{v}_p, \Sigma_p) \quad (9)$$

where

$$\bar{v}_p = \bar{v} + Q(Q^{pT}Q^p + \sigma^2 I_n)^{-1}Q^{pT}(V^p - \bar{v}^p) \quad (10)$$

$$\Sigma_p = \sigma^2 Q(Q^{pT}Q^p + \sigma^2 I_n)^{-1}Q^T \quad (11)$$

Finally, the posterior shape model gets updated (Fig. 2(d)) using the calculated posterior distribution.

### C. Virtual-Physical Fusion for MR Navigation

The initial transformation matrix  $T_{Hol}^{Tra}$  that aligns the HoloLens coordinate system  $\{Hol\}$  with the optical tracker coordinate system  $\{Tra\}$  can be obtained via the interactive calibration procedure (Fig. 2(e)). However, it's usually difficult for surgeons to maintain stability when matching the calibration cube to its virtual counterpart, resulting in the collected  $P_i^{Tra}$  deviating from its target truth. To rectify this, we proposed a hand tremble compensation method to improve the accuracy and robustness of the virtual-physical fusion, which proceeds as follows:

*1) Hand Tremble Compensation:* During the calibration procedure, a series of points were collected continuously during the calibration procedure to estimate the true fiducial central. Let  $S_{Tra} = \{\hat{P}_i^{Tra}, i = 1, \dots, \hat{N}\}$  denote the 3D collected point data set, where  $\hat{N}$  denotes the size of  $S_{Tra}$ . The  $j$ -th closest point of  $\hat{P}_i^{Tra}$  is described as  $\hat{P}_{i,j}^{Tra-close}$ . The normal curvature of  $\hat{P}_i^{Tra}$  relative to  $\hat{P}_j^{Tra-close}$  can be computed as

$$C_j^i = -\frac{\sin \beta}{\left| \overrightarrow{\hat{P}_i^{Tra} \hat{P}_{i,j}^{Tra-close}} \right| * \sin \alpha} \quad (12)$$

where  $\beta$  represents the angle between the normal vector of  $\hat{P}_i^{Tra}$  and the normal vector of  $\hat{P}_{i,j}^{Tra-close}$ , and  $\alpha$  represents the angle between the normal vector of  $\hat{P}_i^{Tra}$  and  $\hat{P}_i^{Tra} \hat{P}_{i,j}^{Tra-close}$ . A total of  $K_{close}$  (here  $K_{close}$  is 4) closest points are used to calculate the average normal curvature of  $\hat{P}_i^{Tra}$ , which can be described as

$$C_i^{Tra} = \left( \sum_{j=1}^{K_{close}} C_j^i \right) / K_{close} \quad (13)$$

Let  $\mu^{Tra}$  denote the average central point of  $S_{Tra}$ . The Euclidean distance between  $\hat{P}_i^{Tra}$  and  $\mu^{Tra}$  is computed as  $d_i^{Tra}$ . We defined a filtering function  $F\{\cdot\}$  to remove the outliers and noises caused by hands trembling. Let  $RS_{tra}$  denote the remaining state of  $\hat{P}_i^{Tra}$ . We define

$$RS_{Tra} = \begin{cases} False, d_i^{Tra} > \omega \bar{d} \text{ and } C_i^{Tra} > \bar{C}^{Tra} \\ True, \text{else} \end{cases} \quad (14)$$

where

$$\bar{d} = \sum_{i=1}^{\hat{N}} d_i^{Tra} / \hat{N}, \quad \bar{C}^{Tra} = \left( \sum_{i=1}^{\hat{N}} C_i^{Tra} \right) / \hat{N} \quad (15)$$

$\omega$  represents the weight of outliers filtering. The bigger  $\omega$  is, the fewer remaining points are. Let  $S_{Rem} = \{\hat{P}_\tau^{Rem}, \tau = 1, \dots, N_{Rem}\}$  denote the remaining collected point data set,

where  $N_{Rem}$  is the size of the  $S_{Rem}$ . The estimated fiducial center  $\bar{P}_i^{Tra}$  can be computed as

$$\bar{P}_i^{Tra} = Cen\{\hat{P}_1^{Rem}, \dots, \hat{P}_{N_{Rem}}^{Rem}\} \quad (16)$$

where  $Cen\{\cdot\}$  denotes the centroid of the remaining collected point data set  $S_{Rem}$ . Each calibration procedure corresponds to  $\bar{K}$  estimated fiducial points (here  $\bar{K}$  is 8). To this end, the estimation calibration matrix  $\bar{T}_{Hol}^{Tra}$  can be expressed as

$$\min \sum_{i=1}^N \left\| (\bar{T}_{Hol}^{Tra})^{-1} * \bar{P}_i^{Tra} - \bar{P}_i^{Hol} \right\|^2 \quad (17)$$

*2) Translation and Rotation Averaging:* Four calibration procedures with hand trembled compensation are performed from different views (front, left, right, ground) to reduce the depth perception error. Four estimation calibration matrices  $\bar{T}_{front}$ ,  $\bar{T}_{left}$ ,  $\bar{T}_{right}$ ,  $\bar{T}_{ground}$  can be obtained, respectively. Each calibration matrix can be described as

$$\bar{T}_i^{Tra-Hol} = \begin{bmatrix} R_i & T_i \\ 0 & 1 \end{bmatrix} (i = 1, \dots, \bar{N}) \quad (18)$$

where  $\bar{N}$  is the number of calibration matrices. The average rotation matrix  $\bar{R}$  is defined as

$$\bar{R} = \arg \min_{R \in SO(3)} \sum_{i=1}^{\bar{N}} d(R_i, R)^2 \quad (19)$$

where  $d\{\cdot\}$  denotes the distance function.

In the Riemannian sense, the average rotation matrix can be computed as [31]

$$\bar{R} = \operatorname{argmin}_{R \in SO(3)} \sum_{i=1}^{\bar{N}} \left\| \operatorname{Log}(R_i^T R) \right\|_F^2 \quad (20)$$

Besides, the average translation  $\bar{T}$  can be computed as  $\bar{T} = \frac{1}{\bar{N}} \sum_{i=1}^{\bar{N}} T_i$ . To this end, the virtual-physical calibration matrix can be expressed as  $\bar{T}_{Hol}^{Tra} = (\bar{R}, \bar{T})$ .

Finally,  $T_{Vir}^{Hol}$  can be obtained via Eq. (1), and the virtual objects can be fused with their physical counterparts in real-time (Fig. 2(f)).

#### D. System Integration for CPS Placement Surgery

To help surgeons observe the subcutaneous anatomical structures, perceive the intraoperative shape of crucial soft tissue, and perform the CPS placement surgery more stably and safely, we integrated the virtual-physical calibration method and soft tissue deformation computing method into our pre-developed MR guided surgical navigation system for orthopedic surgeries [25], [32], [33].

The hardware components of the integrated system are shown in Fig. 3. An external optical tracker (Polaris Vega, Northern Digital Inc., Canada) is used to track objects' poses with a positioning accuracy of 0.35 mm. The US system (DT-7 T, Mindray, China) can provide intraoperative US images by scanning the patient with the US probe (7L4P, Mindray, China). The OST-HMD (HoloLens 2, Microsoft Inc., USA) can provide an MR surgical environment for surgeons wearing it. A 3D-printed calibration cube (WEILAI 8000 resin, Wenext Technology Co., Ltd,

China) is used for virtual-physical calibration. A surgical robot (UR5, Universal Robot, Damark) is used to implement the CPS placement surgery. An electric drill controller (Chiopro 980, Bien-Air, Switzerland) can control the speed and provide power for the drill bit. A workstation with an IntelCore i5-10400F CPU and NVIDIA GTX 1660 GPU is used for computing and communication. The interface of our developed control software is displayed on the external display (37PFL7422, Philips, Netherlands).

We developed an integrated software (Fig. 4) named MR-SNS using some open-sourced toolkits including QT (<https://www.qt.io>), VTK (<https://www.vtk.org>), ITK (<https://itk.org>), statismo (<http://www.statismo.org>), PLUS (<https://plustoolkit.github.io>). MR-SNS software consists of four functional areas. The preparing area is used for date import, registration and calibration. The function area contains functions for the robot, MR, US, and display. The display area is used for model rendering and interaction. Some important parameters are shown on the output area during navigation.

With the integrated system, the surgical workflow for CPS placement surgery can be divided into three steps. Firstly, the virtual-physical calibration procedure is conducted with the hand tremble compensation algorithm. An MR-based surgical scene was then constructed, in which the holographic cervical vertebrae with crucial soft tissues and preoperative planning paths are superposed on their physical counterparts. Secondly, with the intraoperative ultrasound scanning, the posterior shape is computed to update the shape representation of the soft target. Thirdly, under the guidance of MR and US images, the surgeon completes the CPS placement procedure using the surgical robot in a human-robot interactive way.

### III. EXPERIMENTS AND RESULTS

Experiments were designed to evaluate the performance of our proposed algorithms and system. Firstly, the accuracy of the soft tissue computing method was evaluated on the silica gel phantom, and the accuracy of the virtual-physical calibration and fusion method was evaluated by comparative experiments. Secondly, the performance of the integrated system for CPS placement surgery was evaluated by phantom experiments. Finally, we conducted an animal experiment to evaluate the feasibility of the whole system.

#### A. Soft Tissue Computing Evaluation

The experimental setup for soft tissue computing evaluation is shown in Fig. 5(a). Regarding the shape of the human carotid artery, we designed and made a carotid artery phantom with silica gel. The phantom was mounted on a water container via transparent threads, and the phantom's shape could be changed freely by stretching the threads (Fig. 5(b)). In this study, we randomly changed the phantom's shape and performed CT scans 20 times for the phantom. The PCA-based prior model was then generated from a data set consisting of the 20 meshes reconstructed from the CT scans. The node of pre-designed fiducial points  $F_i^{PCA}$  on the PCA model was remarked as  $N_i^{PCA}$  (Fig. 5(d)).

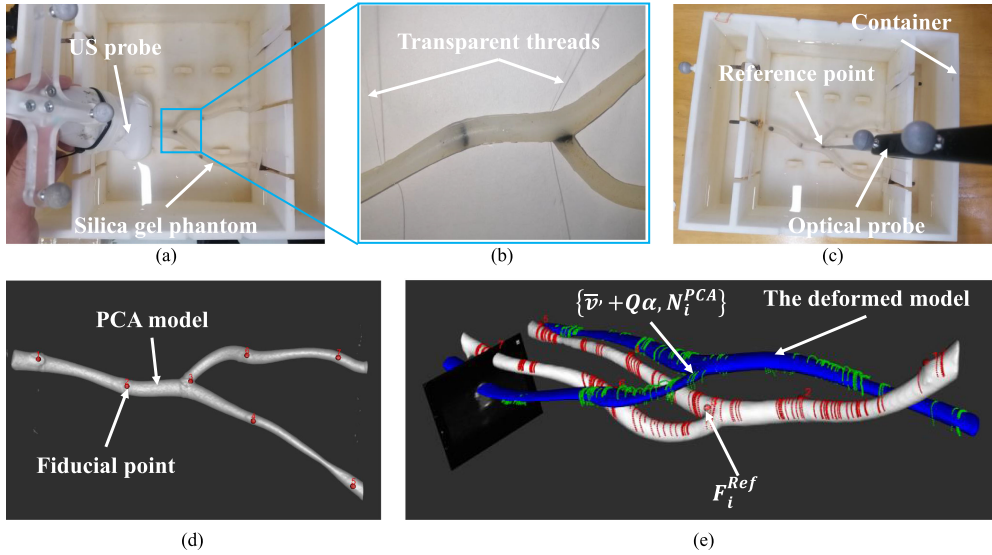


**Fig. 5.** Soft tissue shape computing experiment. (a) The experimental setup. (b) The transparent stretching threads for tissue deformation. (c) Acquisition of the reference points. (d) Location of fiducial points in the PCA model. (e) The deformed PCA model.

The fiducial point error  $E^{FP}$  and the surface distance error  $E^{SD}$  are both defined and used to evaluate the accuracy of the soft tissue computing. After US scanning and soft tissue deformation, the PCA model got updated (Fig. 5(e)) and  $F_i^{PCA}$  were transformed into  $\{Pat\}$ . The position of the pre-designed fiducial points  $F_i^{Ref}$  were obtained by an optical probe, which served as the ground truth (Fig. 5(c)). Then  $E^{FP}$  can be computed as

$$E^{EP} = \frac{1}{N_{FP}} \sum_{i=1}^{N_{FP}} \|F_i^{Ref} - T_{Pre} * Cor\{\bar{v} + Q\alpha, N_i^{PCA}\}\| \quad (21)$$

where  $Cor\{\cdot\}$  denotes the coordinates of  $N_i^{PCA}$  after deformation.  $N_{FP}$  is the number of fiducial points (here is 7).

After deformation, we exported the deformed model as  $M^{Def}$ . Besides, we locked the threads to keep the shape of the phantom unchanged, and another CT scanning was then conducted. The carotid artery from the CT image was reconstructed as the reference mesh  $M^{Ref}$ . Then  $E^{SD}$  can be defined as

$$E^{SD} = SurD\{M^{Def}, M^{Ref}\} \quad (22)$$

where  $SurD\{\cdot\}$  represents the mean surface Euclidean distance between two meshes.

A total of six trials were performed to evaluate the feasibility and accuracy of our proposed posterior shape model based soft tissue computing method. The experimental results for six trials are shown in Table I. The fiducial point error for six cases was  $2.19 \pm 0.21 mm$ , and the mean surface distance error was  $1.52 \pm 0.43 mm$ . The distribution of the surface distance error between  $M^{Def}$  and  $M^{Ref}$  (for case 1) was shown in Fig. 6(b). As a contrast, the distribution of the surface distance error between the original PCA model and  $M^{Ref}$  was shown in Fig. 6(d). On the whole, our proposed method can accurately track the deformation of soft tissues, and its performance is much better than using the rigid PCA model.

**TABLE I**  
SOFT TISSUE COMPUTING EXPERIMENT RESULT

Trials	Fiducial point error (mm)	Maximum surface distance error (mm)	Absolute mean surface distance error (mm)
Case 1	2.33	2.90	$1.44 \pm 0.41$
Case 2	2.21	2.23	$1.06 \pm 0.35$
Case 3	1.90	3.48	$2.07 \pm 0.64$
Case 4	2.23	2.82	$1.41 \pm 0.49$
Case 5	2.47	3.06	$1.99 \pm 0.52$
Case 6	2.02	2.37	$1.12 \pm 0.37$

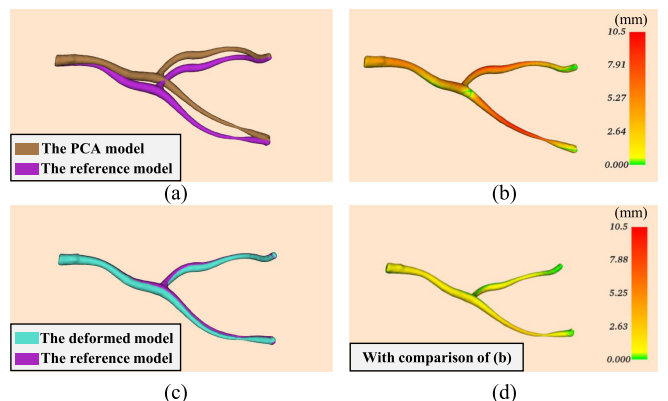


**Fig. 6.** The surface distance error for case 1. (a) The relative position of the original PCA model and the reference model. (b) The distribution of the surface distance error between the original PCA model and  $M^{Ref}$ . (c) The relative position of the deformed model and the reference model. (d) The distribution of the surface distance error between  $M^{Def}$  and  $M^{Ref}$ .

## B. Mixed Reality Calibration and Fusion Evaluation

We designed a comparative experiment to evaluate the accuracy and efficiency of our proposed virtual-physical calibration method. A participant who is familiar with MR technology performed 12 calibration trials with three methods respectively.

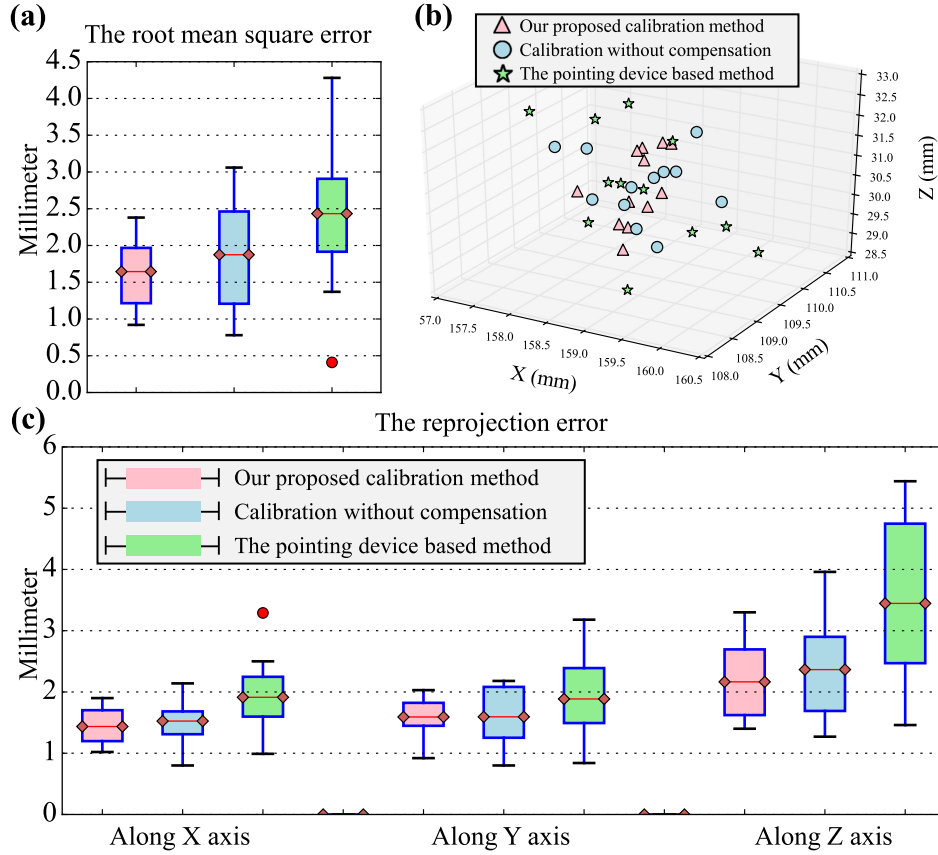


**Fig. 7.** Experimental results of MR calibration. **(a)** The RMS error results of the comparison experiment. **(b)** The spatial distribution of one fiducial marker. **(c)** The reprojection error of the comparison experiment.

The first method was using our proposed virtual-physical calibration with hand trembled compensation, where the participant required to conduct the matching process four times from different views. In the second method, the participant was asked to perform the matching procedure four times from one view without hand trembled compensation. The third method was the pointing device based approach proposed by sun *et al.* [23]. The accuracy of the virtual-physical fusion can be evaluated by calculating the root mean square (RMS) error:

$$E^{RMS} = \sqrt{\frac{1}{n^f} \sum_{i=1}^{n^f} \|P_i^f - (T_{Pat}^{Tra})^{-1} * T_{Hol}^{Tra} * T_{Vir}^{Hol} * P_i^v\|} \quad (23)$$

where  $P_i^f$  represents the fiducial marker's coordinate relative to  $\{Pat\}$ , and  $P_i^v$  represents the virtual fiducial marker's coordinate relative to  $\{Vir\}$ .  $n^f$  is the number of fiducial markers we selected (here is 6). We define the reprojection errors along  $X$ ,  $Y$ ,  $Z$  axes as  $E_X^{proj}$ ,  $E_Y^{proj}$  and  $E_Z^{proj}$ , respectively. The experimental results are shown in Fig. 7.

With an RMS error of  $1.64 \pm 0.48$  mm, our proposed MR calibration method achieved an error reduction of 12.3% compared with calibration methods without compensation, and an error reduction of 32.5% compared with the pointing device based method (Fig. 7(a)). Especially, the standard deviation was

significantly reduced. Compared with calibration methods without compensation, our proposed method achieved no significant improvement in reprojection error along  $X$  axis and  $Y$  axis (Fig. 7(c)). However, the reprojection error along  $Z$  axis was reduced by 8.47% compared with calibration methods without compensation, and by 37.4% compared with the pointing device based method. The time consumption for our proposed method was  $34 \pm 7$  s, which was slightly more than the other two methods. The spatial distribution of one fiducial marker transformed from  $\{Vir\}$  is shown in Fig. 7(b).

### C. Feasibility Evaluation for CPS Placement Surgery

To evaluate the feasibility of the integrated system, a CPS placement experiment was performed on the cervical vertebrae model. The surgical workflow is divided into the following steps:

- 1) the surgeon firstly starts the surgical robot and manipulates it to a proper initial position. The control software is then launched and connected with the optical tracker, the US system, the surgical robot, and the OST-HMD.
- 2) a spatial calibration procedure and a temporal calibration procedure are conducted for the US system. The robotic calibration procedures are then conducted.
- 3) a surface registration procedure is conducted to obtain  $T_{Pat}^{Tra}$ . With the calibration cube, the surgeon completes the virtual-physical calibration manually.

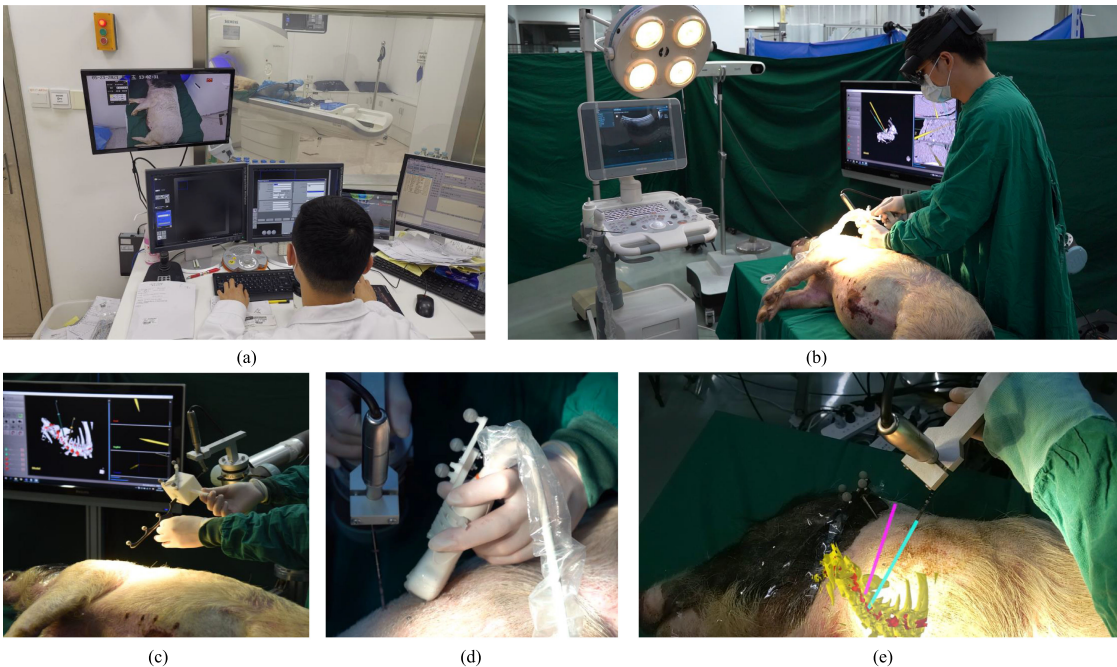


**Fig. 8.** Animal experiment for CPS placement surgery. (a) A CT scanning for the experimental swine. (b) The physical setup. (c) System calibration procedures. (d) Intraoperative US scanning. (e) CPS placement procedure in MR surgical environment.

- 4) the virtual cervical vertebrae with vital soft tissues and planned paths are superposed on the surgical site. And dynamic tracking and navigation are enabled.
- 5) under the guidance of the intraoperative safety strategy, the surgeon completes the CPS placement procedure in a human-robot interactive way.

To evaluate the feasibility and accuracy of the integrated system, a phantom with complete cervical soft and hard tissues (Shanghai Linksunshine Intelligent Technology Co., Ltd, China) was used. Five trials were performed by an orthopedic surgeon with extensive experience in MR and surgical robot. C5 and C6 pedicle screw placement were planned and conducted for each trial. The results illustrated that the average distance and angle deviation [32] were  $1.04 \pm 0.27 \text{ mm}$  and  $1.53 \pm 0.41^\circ$ , respectively. The cervical vertebrae, neurovascular tissue and preoperative planning paths were superposed on the surgical site, and dynamic navigation worked with a delay of  $247 \pm 43 \text{ ms}$ . For all trials, no interference between the drill bit and the critical soft tissues occurred.

#### D. Animal Experiment and Results

After approval by the institutional ethics committee, we further conducted a CPS placement surgery on a Bama miniature swine. As shown in Fig. 8(a), a CT scanning was performed firstly, with  $512 \times 512 \times 425$  voxels and resolution of  $0.7734 \times 0.7734 \times 1 \text{ mm}$ . Based on the preoperative image, both crucial structure segmentation and preoperative surgical planning were then conducted by a senior orthopedic surgeon. Fig. 8(b) illustrates the physical setup for the animal experiment. After conducting offline and online calibration procedures (Fig. 8(c)), the surgeon wearing the OST-HMD performed the

robotic assisted CPS placement surgery. An intraoperative US scanning was continuously conducted to update the shape of the soft tissue (Fig. 8(d)). The drill bit moved accurately along the virtual drilling path under the guidance of the intraoperative safety strategy (Fig. 8(e)).

After surgery, a postoperative CT scanning was conducted. By aligning the postoperative CT image to the preoperative image, the reconstructed postoperative drilling paths were transformed into  $\{\text{Pre}\}$  (Fig. 9). Results indicated that the distance deviations for the two paths were  $1.37 \text{ mm}$  and  $1.58 \text{ mm}$ , respectively. And the angle deviations for the two paths were  $1.24^\circ$  and  $1.79^\circ$ , respectively. The results illustrate that our proposed system can significantly meet the clinical demands.

#### IV. DISCUSSION

Although tremendous progress has been achieved in computer assisted spine surgery, the CPS placement surgery remains challenging due to the complex anatomy structures around the head and neck region. In this study, we proposed a soft tissue deformation tracking method and an improved interactive virtual-physical calibration method, and finally integrated them into the MR guided robotic system.

Compared with traditional surgical navigation systems and surgical robotic systems [34], [35], our proposed system involves significant advantages in the following aspects. Firstly, by constructing an MR surgical navigation environment, the developed system eliminates the hand-eye coordination problem. It benefits surgical safety improvement as surgeons are no longer required to switch views during the operation. Secondly, the deformation of the critical soft tissue can be continuously tracked during the operation, thus potential interference between the soft tissue and

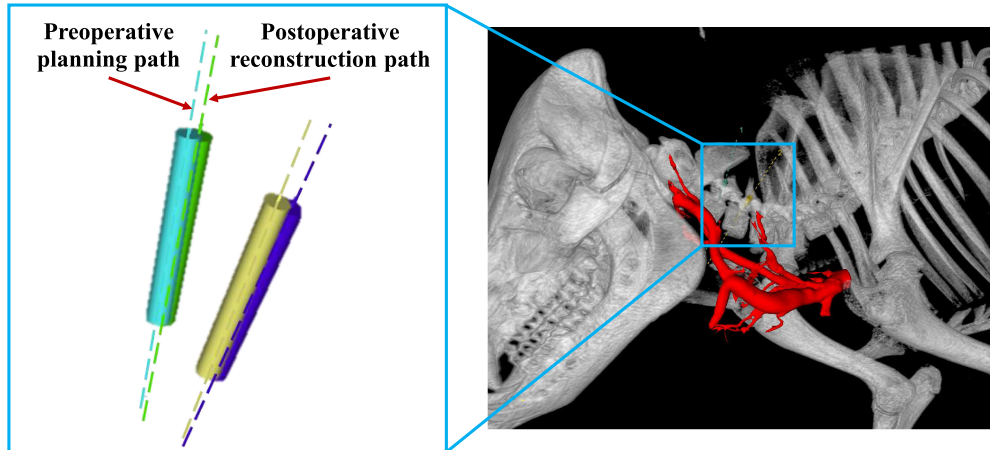


Fig. 9. Accuracy evaluation for the animal experiment.

the surgical instrument can be perceived in advance. This could decrease the risk of critical soft tissue injury intraoperatively. Thirdly, the involvement of US device radically diminish the intraoperative radiation exposure. All virtual objects can be reconstructed based on preoperative CT images and intraoperative real-time US slices.

In our proposed soft tissue deformation computing method, intraoperative US images were segmented to obtain feature points and transformed into the PCA model to obtain intersection points. With continuous US scanning, the posterior distribution can be computed and the soft tissue deformation can be updated in real time. Thus, the dynamic updating problem that restricts the traditional methods can be solved. Phantom experimental results indicated that the average delay of our system was  $247 \pm 43\text{ ms}$ . Two major factors caused this delay. One is the wireless network connection between the PC and the OST-HMD, and the other is the time consumption for US image acquisition and segmentation. The fiducial point and surface distance errors were used to evaluate the accuracy of the proposed deformation computing method. Results illustrated a fiducial point error of  $2.19 \pm 0.21\text{ mm}$ , and a mean surface distance error of  $1.52 \pm 0.43\text{ mm}$ . The deformation computing error is mainly caused by the US image calibration error, the US image segmentation error, and posterior distribution error.

The superimposition accuracy of the virtual tissue and the physical site determines the feasibility of the MR-based surgical navigation system. In this study, we proposed a novel virtual-physical calibration method with hand tremble compensation. By performing the virtual-physical calibration procedure from different views, the average translation and rotation of the final transformation matrix can be computed. Thus, the accuracy and robustness of the virtual-physical fusion were further improved with comparison of existing MR fusion methods [23]. Results indicated that our proposed calibration method achieved an RMS error benefit of 12.3% compared with traditional methods without compensation, and 21.5% compared with the pointing device based method. Also, the reprojection error along Z axis was reduced by 8.5% compared with traditional methods without

compensation, and by 37.4% compared with the pointing device based method. Especially, the standard deviations of RMS error and reprojection error were both reduced. The RMS error of our proposed calibration method was  $1.64 \pm 0.48\text{ mm}$ , which was influenced by the following aspects. Firstly, the SLAM-based positioning algorithm for HoloLens was extremely sensitive to the change of the surgical environment, thus the positioning stability of  $\{\text{Hol}\}$  got limited. Secondly, the interactive calibration procedure for MR included some artificial errors caused by visual fatigue and depth perception problems.

As for future work, we plan to establish a remote desktop relationship between the OST-HMD and the PC. Thus all procedures in the C++ application running on PC can be implemented via hand gestures, and a sterile surgical environment can be guaranteed. Moreover, the performance of the proposed system on real patients will be evaluated, and its clinical acceptance will be investigated.

## V. CONCLUSION

In this study, we developed a mixed reality and intraoperative US image based robotic system for CPS placement surgery with real-time soft tissue computing. Experimental results illustrated that the mean surface distance error for soft tissue deformation was  $1.52 \pm 0.43\text{ mm}$ , and the average distance deviation for CPS placement was  $1.04 \pm 0.27\text{ mm}$ . Our proposed system involves potential advantages over traditional navigation systems in terms of hand-eye coordination and intraoperative safety. Further study will be conducted to evaluate its clinical performance.

## REFERENCES

- [1] F. Guo *et al.*, "Individualized 3D printing navigation template for pedicle screw fixation in upper cervical spine," *Plos One*, vol. 12, no. 2, 2017, Art. no. e0171509.
- [2] B. J. Dunlap, E. E. Karaikovic, H.-S. Park, M. J. Sokolowski, and L.-Q. Zhang, "Load sharing properties of cervical pedicle screw-rod constructs versus lateral mass screw-rod constructs," *Eur. Spine J.*, vol. 19, no. 5, pp. 803–808, 2010.

- [3] N. Shimokawa and T. Takami, "Surgical safety of cervical pedicle screw placement with computer navigation system," *Neurosurgical Rev.*, vol. 40, no. 2, pp. 251–258, 2017.
- [4] A. F. Joaquim, L. Tan, and K. D. Riew, "Posterior screw fixation in the subaxial cervical spine: A technique and literature review," *J. Spine Surg.*, vol. 6, no. 1, pp. 252–261, 2020.
- [5] S. Rajasekaran, P. R. M. Kanna, and T. A. P. Shetty, "Intra-operative computer navigation guided cervical pedicle screw insertion in thirty-three complex cervical spine deformities," *J. Craniovertebral Junction Spine*, vol. 1, no. 1, pp. 38–43, 2010.
- [6] Y. Heo *et al.*, "The learning curve of subaxial cervical pedicle screw placement: How can we avoid neurovascular complications in the initial period?," *Operative Neurosurgery*, vol. 17, no. 6, pp. 603–607, 2019.
- [7] A. Al-Habib, F. Albadr, J. Ahmed, A. Aleissa, and A. Al Towim, "Quantitative assessment of vertebral artery anatomy in relation to cervical pedicles: Surgical considerations based on regional differences," *Neurosciences*, vol. 23, no. 2, pp. 104–110, 2018.
- [8] R. Verma *et al.*, "Functional outcome of computer-assisted spinal pedicle screw placement: A systematic review and meta-analysis of 23 studies including 5,992 pedicle screws," *Eur. Spine J.*, vol. 19, no. 3, pp. 370–375, 2010.
- [9] Y. L. Yang, D. S. Zhou, and J. L. He, "Comparison of isocentric C-arm 3-Dimensional navigation and conventional fluoroscopy for C1 lateral mass and C2 pedicle screw placement for atlantoaxial instability," *J. Spinal Disord. Techn.*, vol. 26, no. 3, pp. 127–134, 2013.
- [10] Y. Ishikawa *et al.*, "Intraoperative, full-rotation, three-dimensional image (O-arm)-based navigation system for cervical pedicle screw insertion," *J. Neurosurgery-Spine*, vol. 15, no. 5, pp. 472–478, 2011.
- [11] S. Chachan *et al.*, "Cervical pedicle screw instrumentation is more reliable with o-arm-based 3D navigation: Analysis of cervical pedicle screw placement accuracy with o-arm-based 3D navigation," *Eur. Spine J.*, vol. 27, no. 11, pp. 2729–2736, 2018.
- [12] R. B. Kochanski, J. M. Lombardi, J. L. Laratta, R. A. Lehman, and J. E. O'Toole, "Image-guided navigation and robotics in spine surgery," *Neurosurgery*, vol. 84, no. 6, pp. 1179–1189, 2019.
- [13] I. H. Lieberman, S. Kisinde, and S. Hesselbacher, "Robotic-assisted pedicle screw placement during spine surgery," *JBJS Essential Surg. Techn.*, vol. 10, no. 2, pp. e0020.1–e0020.15, 2020.
- [14] A. K. Ahmed *et al.*, "First spine surgery utilizing real-time image-guided robotic assistance," *Comput. Assist. Surg.*, vol. 24, no. 1, pp. 13–17, 2019.
- [15] W. Tian *et al.*, "Guideline for posterior atlantoaxial internal fixation assisted by orthopaedic surgical robot," *Orthopaedic Surg.*, vol. 11, no. 2, pp. 160–166, 2019.
- [16] R. J. Hlubek *et al.*, "Safety and accuracy of freehand versus navigated C2 pars or pedicle screw placement," *Spine J.*, vol. 18, no. 8, pp. 1374–1381, 2018.
- [17] J. T. Gibby, S. A. Swenson, S. Cvetko, R. Rao, and R. Javan, "Head-mounted display augmented reality to guide pedicle screw placement utilizing computed tomography," *Int. J. Comput. Assist. Radiol. Surg.*, vol. 14, no. 3, pp. 525–535, 2019.
- [18] F. Chen *et al.*, "Tissue structure updating for in situ augmented reality navigation using calibrated ultrasound and two-level surface warping," *IEEE Trans. Biomed. Eng.*, vol. 67, no. 11, pp. 3211–3222, Nov. 2020.
- [19] G. Samei *et al.*, "Real-time FEM-based registration of 3-D to 2.5-D transrectal ultrasound images," *IEEE Trans. Med. Imag.*, vol. 37, no. 8, pp. 1877–1886, Aug. 2018.
- [20] N. Navab, S.-M. Heinrich, and J. Traub, "Camera augmented mobile C-arm (CAMC): Calibration, accuracy study, and clinical applications," *IEEE Trans. Med. Imag.*, vol. 29, no. 7, pp. 1412–1423, Jul. 2010.
- [21] L. Ma, Z. Zhao, F. Chen, B. Zhang, L. Fu, and H. Liao, "Augmented reality surgical navigation with ultrasound-assisted registration for pedicle screw placement: A pilot study," *Int. J. Comput. Assist. Radiol. Surg.*, vol. 12, no. 12, pp. 2205–2215, 2017.
- [22] F. Liebmann *et al.*, "Pedicle screw navigation using surface digitization on the microsoft HoloLens," *Int. J. Comput. Assist. Radiol. Surg.*, vol. 14, no. 7, pp. 1157–1165, 2019.
- [23] Q. Sun, Y. Mai, R. Yang, T. Ji, X. Jiang, and X. Chen, "Fast and accurate online calibration of optical see-through head-mounted display for AR-based surgical navigation using microsoft HoloLens," *Int. J. Comput. Assist. Radiol. Surg.*, vol. 15, no. 11, pp. 1907–1919, 2020.
- [24] G. Eggers, J. Muhling, and R. Marmulla, "Image-to-patient registration techniques in head surgery," *Int. J. Oral Maxillofac. Surg.*, vol. 35, no. 12, pp. 1081–1095, 2006.
- [25] P. Tu, Y. Gao, A. J. Lungu, D. Li, H. Wang, and X. Chen, "Augmented reality based navigation for distal interlocking of intramedullary nails utilizing microsoft HoloLens 2," *Comput. Biol. Med.*, vol. 133, 2021, Art. no. 104402.
- [26] Z. Zhao, D. Ye, X. Zhang, G. Chen, and B. Zhang, "Improved direct linear transformation for parameter decoupling in camera calibration," *Algorithms*, vol. 9, no. 2, pp. 31.1–31.15, 2016.
- [27] G. Carbajal *et al.*, "Improving n-wire phantom-based freehand ultrasound calibration," *Int. J. Comput. Assist. Radiol. Surg.*, vol. 8, no. 6, pp. 1063–1072, pp. 1063–1072, 2013.
- [28] A. Lasso, T. Hefter, A. Rankin, C. Pinter, T. Ungi, and G. Fichtinger, "PLUS: Open-source toolkit for ultrasound-guided intervention systems," *IEEE Trans. Biomed. Eng.*, vol. 61, no. 10, pp. 2527–2537, Oct. 2014.
- [29] L. A. Groves, B. VanBerlo, N. Veinberg, A. Alboog, T. M. Peters, and E. C. S. Chen, "Automatic segmentation of the carotid artery and internal jugular vein from 2D ultrasound images for 3D vascular reconstruction," *Int. J. Comput. Assist. Radiol. Surg.*, vol. 15, no. 11, pp. 1835–1846, 2020.
- [30] T. Albrecht *et al.*, "Posterior shape models," *Med. Image Anal.*, vol. 12, pp. 959–973, 2013.
- [31] M. Moakher, "Means and averaging in the group of rotations," *SIAM J. Matrix Anal. Appl.*, vol. 24, no. 1, pp. 1–16, 2002.
- [32] Y. Li *et al.*, "Automatic robot-world calibration in an optical-navigated surgical robot system and its application for oral implant placement," *Int. J. Comput. Assist. Radiol. Surg.*, vol. 15, no. 10, pp. 1685–1692, 2020.
- [33] X. Chen *et al.*, "Development of a surgical navigation system based on augmented reality using an optical see-through head-mounted display," *J. Biomed. Informat.*, vol. 55, pp. 124–131, 2015.
- [34] N. Hecht *et al.*, "Intraoperative computed tomography versus 3D C-arm imaging for navigated spinal instrumentation," *Spine*, vol. 43, no. 5, pp. 370–377, 2018.
- [35] R. Schouten *et al.*, "Intra-operative cone-beam CT (O-arm) and stereotactic navigation in acute spinal trauma surgery," *J. Clin. Neurosci.*, vol. 19, no. 8, pp. 1137–1143, 2012.